ATAD2 mediates chromatin-bound histone chaperone turnover

Ariadni Liakopoulou[1], Fayçal Boussouar[1#], Daniel Perazza[1], Sophie Barral[1], Emeline Lambert[1], Tao Wang[1], Florent Chuffart[1], Ekaterina Bourova-Flin[1], Charlyne Gard[2], Denis Puthier[2], Sophie Rousseaux[1], Christophe Arnoult[1], André Verdel[1], Saadi Khochbin[1#]

1- Université Grenoble Alpes, INSERM U1209, CNRS UMR 5309, Institute for Advanced Biosciences, 38000, Grenoble, France

2- Aix Marseille Université, INSERM, UMR U1090, TAGC, Marseille, France

Correspondence:

Saadi Khochbin: saadi.khochbin@univ-grenoble-alpes.fr

Fayçal Boussouar: faycal.boussouar@univ-grenoble-alpes.fr

Abstract

ATAD2, a conserved protein which is predominantly expressed in embryonic stem (ES) cells and spermatogenic cells, emerges as a crucial regulator of chromatin dynamics. Our previous parallel studies in both ES cells and *S. pombe* highlighted the key role of ATAD2 in facilitating chromatin-bound histone chaperone turnover. Focusing on spermatogenesis, we demonstrate here that ATAD2 regulates the HIRA-dependent localization of H3.3 on the genome and influences H3.3-mediated gene transcription. Moreover, by modulating histone eviction and the assembly of protamines, ATAD2 ensures proper chromatin condensation and genome packaging in mature sperm. Disruption of *Atad2* function in mice leads to abnormal genome organization in mature spermatozoa. Together, these findings establish a previously overlooked level of chromatin dynamic regulation, governed by ATAD2's interaction with histone chaperones and chromatin, which controls the balance between histone deposition and removal.

Introduction

Spermatogenesis involves unique and dramatic chromatin remodelling and genome reorganization events that take place in preparation for a shift from the universal nucleosome-based eukaryotic genome organization into a unique nucleoprotamine-based structure (Gaucher et al. 2010; Bao and Bedford 2016; Le Blevec et al. 2020; Okada 2022). During the last decade, important information on the molecular basis of the nucleosome-to-nucleoprotamine transition during the postmeiotic phases of spermatogenesis became available. Several testis-specific H2A, H2B and H3 histone variants replace the canonical histones, locally or globally, at different stages, starting early during the commitment of cells into meiotic and post-meiotic differentiation (Hoghoughi et al. 2018). Most of this nucleosome dismantlement and assembly occurs in the absence of DNA replication. In other words, the replication-independent nucleosome assembly pathways, such as the well-documented HIRA-dependent H3.3 assembly, are expected to be critical in ensuring the necessary chromatin dynamics in these cells. Finally, hints to the functions of transition proteins (TPs), and their functional relationship with protamines (PRMs) were proposed based on the study of a specific late-expressing H2A variant, H2A.L.2 (Barral et al. 2017b). In the proposed model we suggest that TPs do not directly replace histones, but rather could be loaded on open H2A.L.2-containing nucleosomes to control PRM assembly. Nucleosome-to-nucleoprotamine transition also includes a TP-dependent pre-PRM2 processing, histone displacement by PRMs and the structuration of the nucleoprotamine-based genome organization in the mature spermatozoa (Barral et al. 2017b; Rezaei-Gazik et al. 2022).

Taking into account this unique dynamic of post-meiotic cells' nucleosomes, it is expected that these cells massively express generic or germline-specific factors that act on chromatin, including histone acetylating machineries, acetylated histone readers and histone variants and their chaperones, all of which mediate histone and non-histone protein exchanges. More specifically, the replication-independent nature of nucleosome assembly, both in cells undergoing meiosis and in post-meiotic cells, strongly suggests the involvement of the chaperone / histone substrate couple, HIRA and H3.3.

An important part of this replication-independent histone assembly and transitions in the genome organizations occurs in the context of a massive histone H4 hyperacetylation in the haploid spermatogenic cells, spermatids, mediated by NUT-p300/CBP histone acetyltransferase complex (Shiota et al. 2018; Rousseaux et al. 2022). Hyperacetylation of

histone H4, especially, the double acetylation on H4K5K8 in these cells, leads to the binding of H4 by the first bromodomain of BRDT and to histone replacement (Moriniere et al. 2009; Gaucher et al. 2012; Goudarzi et al. 2016; Shiota et al. 2018). Additionally, Histone H4 hyperacetylation, especially at K5, could also be recognized by another bromodomain-containing factor of unknown function in spermatogenic cells, ATAD2 (Caron et al. 2010; Morozumi et al. 2016).

ATAD2 is a highly conserved bromodomain-containing factor harbouring, in addition, an AAA ATPase domain (Boussouar et al. 2013; Cattaneo et al. 2014). Our early work showed that Atad2 is predominantly expressed in embryonic stem cells (ES cells), as well as in spermatogenic cells, and is aberrantly activated in virtually all solid cancers (Caron et al. 2010). Although ATAD2's function in cancer prompted many investigations (Liu et al. 2022), its function in its physiological context of expression has remained largely overlooked. We reported the first investigations of ATAD2's function in embryonic stem cells (Morozumi et al. 2016). These studies in ES cells showed that ATAD2 is recruited into acetylated transcriptionally active chromatin and is critical to keep the chromatin of ES cells highly dynamic, as illustrated by an ATAD2-dependent high rate of histone exchange (Morozumi et al. 2016). Later parallel studies by our laboratory, in ES cells and in *S. pombe*, deciphered the molecular basis of this activity of ATAD2, which relies on its capacity to ensure the turnover of the chromatin-bound histone chaperone, HIRA and FACT (Wang et al. 2021). In addition to ES cells, *Atad2* is also highly expressed in male germ cells, pointing to its potential role in the regulation of HIRA -dependent H3.3 assembly in these cells, especially, in post-meiotic cells. Indeed, previous published works have highlighted the important function of H3.3 assembly in meiotic and post-meiotic male genome programming (van der Heijden et al. 2007; Yuen et al. 2014; Tang et al. 2015; Fontaine et al. 2022). We therefore hypothesized that ATAD2-controlled HIRA-H3.3 activity would also be a critical player in post-meiotic male genome reorganization, as HIRA has been shown to be essential post-fertilization (Lin et al. 2014) and during oogenesis (Nashun et al. 2015).

Using a lacZ reporter *Atad2* KO mouse model, we could show that *Atad2*'s expression is dramatically enhanced in post-meiotic male germ cells, ensuring a proper dynamics of histone H3.3, including on the sex chromosomes. More remarkably, our data demonstrate that ATAD2 controls the appropriate expression of a series of genes whose activity is known to be H3.3-dependent in post-meiotic cells. Additionally, in the absence of ATAD2, perturbed nucleosome

dynamics leads to a delayed histone-to-PRM-replacement, leading to a defective global final male genome compaction. Although this defective mature spermatozoon genome compaction has little effect on male fertility following natural reproduction, it impacts the success of *in vitro* fertilization using spermatozoa from *Atad2* KO mice pointing to a more fragile genome in these cells.

In summary, our work identified a yet unknown level of the regulation of chromatin plasticity, that involves the control of histone chaperone dynamics, particularly that of HIRA, controlling the proper male germ cell transcriptional regulation, genome compaction and optimal male fertility.

Results

Atad2 is predominantly expressed in haploid male germ cells

Atad2 is normally expressed in ES and spermatogenic cells and remains silent in the majority of adult tissues (Morozumi et al. 2016). Therefore, in addition to ES cells, male germ cells constitute the second cell type where the molecular basis of the physiological ATAD2 activity could be investigated.

To decipher the function of ATAD2 during spermatogenesis, we used a mouse model harboring an insertion of a *lacZ* reporter cassette between exons 11 and 12 that enables fusion of the *lacZ* transgene with exon 11 of the long form of *Atad2* (**Fig.1A**) and production of a non-functional ATAD2-lacZ fusion protein (**Fig. 1B**), referred to as ATAD2 KO in this study. Furthermore, we crossed these mice with transgenic mice expressing ubiquitously Cre recombinase under *CMV* promoter, in order to remove the *neo* cassette and to delete *Atad2's* exon 12 (**Fig. 1B**). In addition to the long somatic form of ATAD2, ATAD2L, the mouse testis encodes a short germ-cell specific isoform that we previously named ATAD2S (Caron et al. 2010). The combined LacZ fusion and *Cre recombinase*-dependent deletion of *Atad2's* exon 12 make both ATAD2L and ATADS indetectable (**Fig. 1C**).

The expression of *lacZ* under the control of the *Atad2* promoter allows one to visualize *Atad2* gene activity in a stage-specific manner. X-gal staining of seminiferous tubule sections from *Atad2* KO mice showed a remarkably high expression of *Atad2* in post-meiotic spermatogenic cells (**Fig. 1D**). It is noteworthy that no staining was observed in the wild-type tubules.

ATAD2 controls HIRA accumulation

In our previous work performed in both *S. pombe* and mouse ES cells, we demonstrated the crucial role for ATAD2 in HIRA-dependent histone dosage as well as in HIRA-chromatin interaction. Among other discoveries, this work showed that in the absence of ATAD2, HIRA becomes trapped on chromatin leading to its accumulation in ES cells, as well as in a variety of cancer cell lines (Wang et al. 2021). Because of this very conserved action of ATAD2 in controlling the HIRA activity, we reasoned that the ATAD2-dependent HIRA activity should be particularly active during spermatogenic cell differentiation, especially, in post-meiotic cells, when ATAD2 expression is highly induced (**Fig. 1D**). To test if the absence of ATAD2 could lead to the accumulation of HIRA, as we previously reported in other systems, we quantified HIRA in spermatogenic cells from both wild-type and *Atad2* KO mice. These investigations revealed an accumulation of HIRA protein in *Atad2* KO spermatogenic cells (**Fig. 2A**), consistent with its increased association with chromatin (Wang et al. 2021). We have also monitored HIRA accumulation as a function of spermatogenic cells stages. Because of the dramatic activation of *Atad2* after meiosis, in spermatids (**Fig.1D**), the ATAD2-dependent accumulation of HIRA was expected to mostly occur in post-meiotic cells. Accordingly, we also compared HIRA accumulation in fractionated spermatogenic cell extracts. This experiment demonstrated that, in the absence of functional ATAD2, the accumulation of HIRA primarily occurs in round spermatids (**Fig. 2B**). This finding is consistent with the post-meiotic activation of Atad2 and its role in regulating the turnover of chromatin-bound HIRA.

ATAD2 controls HIRA-dependent H3.3 localization and H3.3-dependent transcription

We speculated that an increased presence of HIRA on chromatin in the absence of ATAD2, should also be associated with increased amounts of deposited histones. Indeed, we have demonstrated previously in *S. pombe* that histone gene inactivation could rescue the growth arrest due to the absence of *Atad2*/*Abo1.* In parallel, we found that in ES cells, in the absence of ATAD2, an increased nucleosome assembly occurs, even on the so-called nucleosome-free region (NFR) (Wang et al. 2021).

Interestingly, visualization of H3.3, the major target of HIRA by immunofluorescence in *Atad2* KO round spermatids, displayed a diffuse, intense staining (**Fig. 3**), which is normally concentrated on the sex chromosomes. (van der Heijden et al. 2007; Fontaine et al. 2022). Indeed, as expected and previously reported, in the wild-type round spermatids, H3.3 was

mostly observed in a single domain, close to the unique chromocenter in these cells (**Fig. 3**, left panels). In the absence of ATAD2, in agreement with an increased residence time of HIRA on chromatin in general and a reduced H3.3 turnover, an increased level of H3.3 could be observed on the sex chromosome (adjacent to the chromocenter), and more interestingly, on all over the genome (**Fig. 3**, right panels).

General chromatin accessibility and transcriptional regulation by ATAD2

H3.3 is known to be dynamically incorporated on a group of active genes, especially around their transcriptional start sites (TSS) (de Dieuleveult et al. 2016). We therefore predicted that the observed increased H3.3 residence time in the absence of ATAD2 would decrease TSS regions' accessibility specially those of highly active genes. To verify this prediction, we purified round spermatid fractions from wild-type and *Atad2* ko mice testes and measured the general chromatin accessibility following an ATAC-seq approach. Chromatin accessibility was then assessed around the TSS of genes, which were categorized into four groups based on the quartile of their mean expression from three independent transcriptomes of wild-type round spermatids (**Fig. 4A**), from the top 25% most highly expressed genes (group 1) to the 25% least expressed genes (group 4). As predicted, the absence of ATAD2 was associated with a significant decrease in TSS region accessibility of the most active genes (**Fig. 4B and 4C**), supporting a role for ATAD2 in maintaining chromatin dynamics at the most highly active chromatin regions.

To visualize the genes more sensitive to ATAD2-mediated chromatin dynamics affecting transcription, we monitored whole genome transcriptional activity during the first spermatogenic wave at day 20 post-partum (PP), when meiosis is complete, and the first post-meiotic cells appear on 22-, 24- and 26-days PP.

In order to definitively confirm our working hypothesis on the ATAD2-HIRA-H3.3 functional interaction, we took advantage of published H3.3-dependent transcriptomic data (Fontaine et al. 2022). Indeed, the authors of this publication identified a series of genes that are mis-regulated in cells with inactivated *H3.3b* gene. Because of the post-meiotic major activation of *Atad2*, we specifically focussed on the gene lists that show a H3.3-dependent deregulated expression in post-meiotic round spermatids.

In these transcriptomes, we specifically followed the expression of the published lists of genes that are downregulated or upregulated in the absence of H3.3 (Fontaine et al. 2022). Very interestingly, we observed that the majority of genes that were reported to be down-regulated in the absence of H3.3 (H3.3-activated genes), are upregulated in the absence of ATAD2, particularly at day 26 PP, when a significant number of post-meiotic cells are present in the testes (**Fig. 5A**, left and middle panels). Gene Set Enrichment Analysis (GSEA) applied to genes that are differentially expressed between wild-type and Atad2 KO cells at day 20 PP, confirmed that the "H3.3-activated" gene set (corresponding to the published list of H3.3-activated genes) are clearly enriched in Atad2 KO cells (**Fig. 5A**, right panel).

This regulation can also be observed when we considered the published list of genes that were up-regulated in the absence of H3.3 (H3.3-repressed genes). In this case, the absence of ATAD2 led to the enhancement of their down-regulation. In other words, the absence of ATAD2 led to an enhancement of H3.3-dependent gene repression (**Fig. 5B**).

Fontaine and colleagues also reported that sex chromosome-linked genes that normally undergo Meiotic Sex Chromosome Inactivation (MSCI), were up-regulated in the absence of H3.3, indicating that H3.3 is required for their repression. We also investigated these genes and showed that they present an enhancement of repression in the absence of ATAD2 (**Fig. 5C**).

These analyses clearly indicate that the absence of ATAD2 enhances H3.3 functions in agreement with increased residence time of H3.3 in nucleosomes. Genes that require H3.3 to be repressed or activated present an enhanced repression or activation, respectively, in the absence of ATAD2.

Overall, these investigations remarkably confirmed a role for ATAD2 in regulating H3.3 function.

ATAD2 is required for controlled histone eviction and PRM assembly

ATAD2's involvement in HIRA-chromatin interaction dynamics and its role in H3.3 assembly in post-meiotic cells, along with its similar function in the dynamics of other histone chaperones like FACT (Wang et al. 2021), led us to investigate whether ATAD2 participates in controlling the histone-to-protamine replacement occurring later in these cells. The histone eviction process involves a genome-wide histone H4 hyperacetylation (Shiota et al. 2018) and a TP-mediated PRMs assembly, which directs histone eviction and the final packaging of the male

genome (Barral et al. 2017a). To test the involvement of ATAD2 in spermatogenic cell chromatin reorganization, we sought to co-detect testis-specific H2B variant, TH2B (Montellier et al. 2013), along with transition protein 1 (TP1) and protamine 1 (PRM1). TH2B is first expressed at the commitment of spermatogenic cells into meiotic divisions and progressively becomes the major H2B species of spermatogenic cell chromatin in the subsequent stages (Montellier et al. 2013). As expected, the accumulation of TP1 and PRM1 in wild-type cells is associated with the eviction of the majority of histones, reflected by the mutually exclusive labelling of TH2B and TP1/PRM1 in distinct cells (**Fig. 6A** and **6B**, Atad2 wild-type mice). In contrast, in *Atad2* KO cells, TH2B and TP1/PRM1 were co-detected in a significant number of cells (**Fig. 6A** and **6B**), suggesting that the process of histone eviction is disturbed. However, in Atad2 KO cells, the initial delay in histone removal is transient, as spermatids with high levels of transition protein TP1 and PRM1 eventually appear (**Fig. 6**).

These observations strongly suggest that, in the absence of ATAD2, the process of histone eviction is also slowed down or delayed, allowing for the simultaneous detection of histones and histone-replacing proteins in the same cells.

Given that NUT-CBP/p300-dependent H4 hyperacetylation, along with the expression of H2A.L.2, TPs, and PRMs, is essential for histone removal, we also investigated whether the observed delay in histone removal is due to defective histone acetylation, particularly at H4K5, as well as disrupted cell type-specific expression and localization of H2A.L.2, TPs, and PRMs. Immunohistochemical detection of H4K5ac, TP2, PRM1, and PRM2 revealed a similar pattern and cell type-specific expression of the investigated proteins when comparing Atad2 KO and wild-type post-meiotic cells. (**Fig. S1**).

These data support the idea that the perturbed modified dynamics of histone/TP/PRM chaperones does not grossly affect the other molecular events involved in the histone-to-PRM replacement.

Perturbed pre-PRM2 processing in the absence of ATAD2

We have shown previously that the H2A.L.2-dependent process of incorporation of TPs into nucleosomes is required for the proper processing of pre-PRM2. The abnormal overlapping staining of histones, TP and protamines observed by immunofluorescence in *Atad2* KO cells, suggested that TPs may not effectively mediate the pre-PRM processing. To test this

hypothesis, we took advantage of our specific pre-PRM2 antibody (Rezaei-Gazik et al. 2022) to investigate pre-PRM2 maturation and assembly. **Figure 7A** shows that although pre-PRM2 is present in both wild-type and *Atad2* KO elongating spermatids, in the absence of ATAD2, pre-PRM2 tends to form dense aggregates as well as fragmented genomic domains. This phenomenon is also associated with an increased accumulation of pre-PRM2 protein level in testis extracts of *Atad2* KO spermatogenic cells compared to wild-type cells as revealed by ELISA (**Fig. 7B**).

These data provide strong evidence that ATAD2 is required to streamline the activity of histone chaperones as well as of factors involved in histone exchange and TP/PRM assembly.

Defective mature spermatozoa genome organization and male fertility *in vitro*

We show that although the *Atad2* KO post-meiotic cells' defective chromatin organization does not affect the testis histology (**Fig. S1** and **data not shown**), it impairs testis weight and sperm count, which are significantly reduced in *Atad2* KO mice (**Fig. S2**).

As expected, the impact of ATAD2 on HIRA function and TP/PRM assembly also has an impact on proper sperm genome compaction. Indeed, mature sperm genome decompaction test revealed a significant difference in the ability of the genome to resist genome decompaction conditions between wild-type Atad2 and *Atad2* KO spermatozoa (**Fig. 8A**). Given that spermatozoa with defective genome compaction are known to have poor success in *in vitro* fertilization (Bashiri et al. 2021), we expected that spermatozoa from Atad2 KO mice would perform worse in *in vitro* fertilization assays compared to wild-type spermatozoa. **Figure 8B** shows that this is, in fact, the case. However, surprisingly, fertility tests carried out on sexually mature adult males revealed that *Atad2* KO male mice are fertile, with only a statistically non-significant effect observed on their ability to foster pups (**Fig. 8C**), indicating that *in vivo* fertilization could buffer a relatively large series of sperm genome compaction defaults.

Discussion

Taking advantage of the very conserved structural features of ATAD2 and relying on the power of yeast genetics, we previously discovered that ATAD2's function is mostly to control major histone chaperone functions. Using a screen of the Abo1/ATAD2-dependent arrest of *S. pombe* cell growth, we found that impressively, 11 of the 14-growth arrest suppressor strains that we isolated, impacted histone chaperones or histones themselves, with 8 distinct

inactivating mutations in the histone chaperone HIRA complex. Furthermore, investigation of ATAD2-depleted mouse ES cells showed that HIRA accumulates and remains bound to nucleosomes, leading to nucleosome overloading around active gene TSSs and on the normally nucleosome-free regions (NFRs) of these genes.

Here, we showed that *Atad2* is highly expressed in post-meiotic spermatogenic cells and that in its absence, as in ES cells and in different cancer cells, HIRA accumulates. Our new data suggest that in the absence of ATAD2 activity, HIRA residency time on chromatin increases leading to decreased dynamics and overloading of its substrate, the histone variant H3.3. This replication-independent histone has been first shown to assemble on the transcriptionally inactive meiotic cell sex chromosomes by Peter de Boer's laboratory (van der Heijden et al. 2007). Subsequent studies showed that H3.3 remained enriched on the sex chromosomes also in early post-meiotic cells, usually localized close to the unique large chromocenter in these cells (Fontaine et al. 2022).

In agreement with the proposed role for ATAD2 in the control of HIRA-dependent dynamics of H3.3, we observed a more intense labelling of H3.3 on the sex bodies in round spermatids and impressively, an increase in the genomic background detection of H3.3 in these cells.

The role of ATAD2 in the HIRA/H3.3 functions is further clearly supported by comparing the reported H3.3-dependent transcriptome with the ATAD2-dependent transcriptome identified here.

Indeed, in the absence of ATAD2, we observed an enhancement of H3.3-dependent gene regulatory events (activation or repression), in agreement with an increased H3.3 presence and hence function, in the chromatin of *Atad2* KO post-meiotic cells.

These investigations on ATAD2's role in post-meiotic spermatogenic cells built upon our previous findings in *S. pombe* and ES cells, uncover an additional level of regulation of histone dynamics, that relies on the dynamics of histone chaperone - chromatin interaction. Previously, A. Groth's laboratory discovered that histone chaperone DNAJC9 recruits the ATPase HSP70 to provide the necessary energy to release the chaperone from chromatin (Hammond et al. 2021). Considering our data on the role of the ATPase ATAD2 with respect to HIRA and that of HSP70 with respect to DNAJC9, it is tempting to propose that ATP energy is required for the proper function of histone chaperones in controlling histone turnover.

Interestingly, very recently, Song laboratory demonstrated that the *S. pombe* Abo1/ATAD2, is required for ATP-dependent dissociation of the histone chaperone FACT from chromatin,

particularly at TSSs (Jang et al. 2024). In line with this conclusion, ChIP-seq mapping of FACT in Atad2-depleted ES cells revealed an accumulation of nucleosome-bound FACT at the TSSs of active genes (Wang et al. 2021), supporting the idea that ATAD2 not only regulates the dynamics of histone-bound HIRA but also that of other histone chaperones such as FACT

In addition to histones, many chromatin-bound regulatory factors also need to dynamically interact with chromatin and hence ATAD2 could also be involved in mediating the dynamic interactions of such chromatin-bound factors. In agreement with this hypothesis, using proteomics of ATAD2-bound nucleosomes in ES cells, we previously co-purified various chromatin bound factors (Morozumi et al. 2016). Other AAA ATPase factors such as p97/VCP, have also demonstrated actions in the dynamics of chromatin-bound factors. Indeed, the AAA ATPase factor, p97/VCP, has been shown to remove H3 variant CENP-A (van den Berg et al. 2023), the chromatin trapped PARP1 (Krastev et al. 2022), trapped Ku70/80 (van den Boom et al. 2016), DNA damage sensors, DDB2 and XPC (Puumalainen et al. 2014), RNA pol II (Lafon et al. 2015), and other chromatin interacting factors. Similarly, ATAD2 AAA ATPase very likely acts on other chromatin-bound factors than histone chaperones. However, in contrast to p97/VCP, and due to its bromodomain , ATAD2 would preferentially act on H4K5 acetylated chromatin regions and would specifically ensure the dynamics of H4 acetylated chromatin-bound factors. Based on the data presented here, we can also include, a role for ATAD2 to streamline steps involving the H2A.L.2-dependent recruitment of TPs and protamine assembly and the final histone displacement in spermatids. The chaperones responsible for TP/PRM assembly are not yet identified, but it is possible that ATAD2 plays a role in dissociating these chaperones from their substrate proteins after the assembly process. That is why in our *Atad2* KO spermatids, we observed an overlap between TP/PRM and histones. This could be due to the delayed removal of chaperones bound to TPs and PRMs and the inability of pre-PRM2 to be processed and hence of PRMs to efficiently replace histones. Since histone replacement still occurs in the absence of ATAD2, it suggests that other AAA ATPases, such as p97/VCP, may compensate for its function. However, under these conditions, although most of the histone replacement takes place, our functional tests such as *in vitro* chromatin decompaction and *in vitro* fertilization, strongly suggest that mature spermatozoa genome organization is not fully complete and the spermatozoa nuclei remain fragile and sensitive to external assaults.

In summary, the functional analysis of ATAD2 during its physiological expression in the post-meiotic phases of spermatogenesis supports our previous conclusions regarding its role in ES cells and its conserved activity in *S. pombe*. Together, these studies reveal a novel layer of regulation in histone turnover and chromatin dynamics, based on the control of histone-bound histone chaperone release .

Materials and Methods

Animal care and breading

Mice were housed at the Grenoble High Technology Animal Facility (PHTA). Mice were euthanized following a procedure approved by the official ethic committee of the University Grenoble Alpes (COMETH, C2EA-12). The investigators directly involved in care and breading of mice had an official animal-handling authorization obtained after 2 weeks of intensive training and a final formal evaluation.

Generation of *Atad2*-KO mice

Atad2 KO mice were obtained from the International Knockout Mouse Consortium, the Welcome Trust Sanger Institute, UK. The 'knockout-first' allele (tm1a) contains an IRES: *lacZ* trapping cassette and a floxed human β-actin promoter-driven *neo* cassette inserted into the intron 12 of the *Atad2* gene (Skarnes et al. 2011). We created $Atad2^{\Delta\, Neo\text{-}Exon\ 12}$ mice by crossing mice bearing the *tm1a* allele with mice expressing Cre recombinase under the control of a ubiquitous human promoter CMV. This cross results in an $Atad2^{LacZ\Delta Neo\text{-}Exon12}$ knockout mouse with the first 11 exons of Atad2 being fused to β-gal, leading to a non-functional Atad2 protein depleted of its bromodomain and AAA ATPase domain.

For *Atad2* KO mice genotyping, multiplex PCR was used to detect LacZ cassette producing a 393-bp WT band and a 293-bp mutant band using primers Atad2_84231_F, TATCCAACAAGCCTGAGCCC, Atad2_84231_R, CAACTGGAGCTGGGTCTTCC and Cas-R, TCGTGGTATCGTTATGCGCC.

Fertility test

Fertility tests were carried out with sexually mature 3-month-old males. Five WT males and five *Atad2* KO males were crossed with two C57BL6 females each, during 3 months, and the litter sizes were monitored during this period.

In vitro Fertilization

Eggs were obtained from 6- to 7-week-old superovulated C57/BL6J females, stimulated by a first injection of 7.5 UI of PMSG (Pregnant Mare Serum Gonadotropin), followed 48 hours later by a second injection of 7.5 UI of HCG (Human Chorionic Gonadotropin). Fourteen hours later,

females were euthanized by cervical dislocation and cumulus-oocytes complexes (COCs) released from the ampulla were collected in 500 µL M2 medium. Spermatozoa from wild type and *Atad2* KO males were harvested by dilaceration of the cauda epididymitis and allowed to swim in 1 mL M2 medium for 10 min at 37°C. Two hundred microliters of sperm were transferred into 800 µL M16 /2% BSA and capacitated for 80 min at 37°C /5% CO_2. Finally, 300,000 sperm were simultaneously added to the COCs and incubated in M16 medium at 37°C /5% CO_2. After 4 hours of incubation, unbound spermatozoa were removed by 3 successive washes with 500 µL of M16. Twenty-four hours after fertilization, unfertilized eggs and two-cell embryos (as an indication of successful fertilization), were scored.

Protein extraction and Immunoblotting

Proteins were extracted in Urea 8M, sonicated for 150J with a probe sonicator, mixed with 4x Laemli loading buffer and heated for 5 minutes at 95 °C. Protein samples were loaded on 4-12% Bis-Tris gels and migrated at 150 V for 1h30. The transfer step was realized using a nitrocellulose membrane with the Bio-Rad Transfer Turbo machine. Nitrocellulose membrane was blocked in 5% milk PBS-Tween 0.1% solution, washed 3 times for 10 minutes with PBS-Tween 0.1% solution and incubated overnight at 4°C with specific antibodies listed in Table S1. Membranes were washed 3 times for 10 minutes with PBS-Tween 0.1% solution and were incubated with HRP secondary antibodies at 1/10000 dilution for 1h at RT under agitation. Revelation was performed using ECL substrates and visualization was performed with the Vilber Fusion FX Chemiluminescence imaging system (Vilber).

ELISA

Urea protein extracts were diluted in PBS and used to coat 96-well round bottom plates by incubating at 4°C overnight. Coating solution was removed and wells were washed 3 times with washing buffer (BSA 1%, PBS-T 0,1%). Wells were blocked with blocking buffer (5% BSA in PBS-T 0,1%) for 2 hours at room temperature under agitation. Blocking buffer was removed and wells were washed 2 times with washing buffer. Primary antibodies for pre-PRM2 (1:1000) and tubulin (1:5000) were diluted into blocking buffer, pipetted into their corresponding wells and incubated overnight at 4°C under mild agitation. Wells were washed 4 times with washing buffer and subsequent incubation with secondary HRP antibodies, diluted 1:5000 in blocking

buffer, was performed for 1 hour at room temperature under mild agitation. Wells were washed 4 times with washing buffer, and TMB ELISA Substrate was added to wells and incubated until the color developed, at which time Stop Solution was added to the wells to stop the reaction. The signal was quantified using a plate reader at 450nm.

X-Gal staining

Male mice were euthanized by cervical dislocation. Testes were dissected out, drilled in 3 points and incubated overnight at 4°C under agitation in fixative solution (0.5% glutaraldehyde, 2 mM $MgCl_2$ and 5 mM EGTA in PBS). After incubation until equilibration in an equilibration buffer (30% sucrose, 2 mM $MgCl_2$ and 5mM EGTA in PBS), testes were frozen individually in OCT on dry ice. Frozen blocks were sectioned at 10 µm slices on Superfrost™ slides and let dry overnight. Slides were fixed with fixation buffer (0.2% glutaraldehyde, 100 mM $MgCl_2$ and 5 mM EGTA in PBS) for 10 min, washed with washing buffer (PBS, 0.02% NP-40, 0.01% Sodium deoxycholate and 2 mM $MgCl_2$) for 5min and incubated three times in 50% Ethanol for 5 min each. Then the slides were stained with staining solution (2 mM $MgCl_2$, 0.02% NP-40, 0.01%Na Doc, 5 mM potassium ferricyanide, 10 mM potassium ferrocyanide and 0.5 mg/ml X-gal) in a wet chamber for several hours at 37°C. The slides were then washed with washing buffer for 5 min and with distilled water, and a counterstaining was performed with hematoxylin. Finally, the slides were washed with running tap water for several minutes and mounted with Dako fluorescent mounting medium.

Immunofluorescence staining of germ cells

Staged seminiferous tubules were prepared as detailed in Gaucher et al. 2012. In order to permeabilize the cells, the slides were then placed in 0.5% saponin, 0.2% Triton X-100, and 1 × PBS at RT for 15 min and washed for 5 min with PBS. The preparations were then incubated in 5% milk, 0.2% PBS-Tween blocking buffer, at RT for 30 min under agitation. The primary antibodies were diluted in 1% dry milk, 0.2% PBS-Tween buffer. The slides were incubated overnight with this diluted solution of the primary antibodies in a humidified chamber at 4°C and then washed three times for 5 min each in the antibodies' dilution buffer. The secondary antibodies were diluted at 1:500 in the same buffer and incubated in a humidified chamber for 30 min at 37°C, and then washed as for the primary antibodies. The DNA was counterstained by Hoechst, and the slides were mounted using Dako fluorescent mounting

medium.

Sperm decompaction test

Spermatozoa from wild type and *Atad2* KO males were harvested by dilaceration of the cauda epididymis and allowed to swim in 1 mL M2 medium for 10 min at 37°C. The sperm-containing suspension was transferred into a 1.5 ml tube and centrifuged at 3000 rpm for 8 min in 4°C. The sperm pellets were resuspended in PBS and dropped onto glass slides to spread and dry at RT. The decompaction mix (50 mM DTT, 400 IU/ml heparin, 0.2% Triton in PBS) was added to each dried sperm drop for 2 min and the decompaction was stopped by placing the slides in 4% PFA for 15 min. After washing with PBS for 5 min, the slides were stained with DAPI and mounted using Dako fluorescent mounting medium. Fluorescent images were captured by a Zeiss inverted microscope under a 63X numeric aperture oil-immersion lens (Carl Zeiss). The size of spermatozoa heads was calculated with ImageJ software.

Spermatogenic cell fraction purification

Spermatogenic cell fraction purification was performed as previously described (Shiota et al. 2018).

ATAC-seq and data analysis

Library preparation

Frozen nuclei from four biologically independent purified spermatid fractions were centrifuged at 3000 g for 5 minutes and then washed in a 1% BSA-PBS solution. Libraries were then prepared from 100,000 nuclei using the ATAC-seq Kit (Catalog No. 53150) from Active Motif, following the manufacturer's protocol (version B9). After quality control (QC) with Qubit and Fragment Analyzer, libraries were subsequently purified using AMPure XP (Beckman Coulter, Catalog No. A63881) beads with a double size selection of 100-800 bp fragments. After a second round of library QC (Qubit and Fragment Analyzer) we performed a paired-end sequencing on a NextSeq 2000 device using a 200-cycle P2 flow cell.

Trimming

The raw fastq files were processed by 5' end trimming, keeping 30bp-length fragments, using fastx_trimmer [http://hannonlab.cshl.edu/fastx_toolkit/. Accessed 28 Feb. 2022.], with options -l 30 -Q33.

Alignment

The trimmed fastq files were aligned on the UCSC Mus_musculus mm10 genome using the Bowtie2 aligner (Langmead and Salzberg 2012), with options –end-to-end, –no-mixed, –no-discordant.

Normalization

The big wig files (.bw) containing normalized integrated aligned read count signals were obtained from by normalizing and smoothing bam files using bamCoverage (from deepTools suite (Ramirez et al. 2014) with options: –binSize 4 –minMappingQuality 30 –normalizeUsing RPM.

Heatmap

The normalized ChIP signal were converted into a 10bp bin matrix of the signal 500b upstream and 1500b downstream protein-coding genes TSS, using computeMatrix (from deepTools suite (Ramirez et al. 2014), with options reference-point -R mm10_pc.bed –referencePoint TSS –binSize 10 –beforeRegionStartLength 500 –afterRegionStartLength 1500

Heatmaps were generated using plotHeatmap (deepTools suite (Ramirez et al. 2014).

RNA-seq data processing

Wild-type (WT) and *Atad2* knockout (KO) homozygous male pups were sacrificed by cervical dislocation on days 20-, 22-, 24-, and 26- postpartum (PP), after which their testes were harvested. RNA was extracted using TRIzol™ reagent, followed by DNA digestion with DNase I. The resulting RNA samples were used for RNA sequencing. For both WT and KO mice, the biological replicates included 3 samples for D20, 4 samples for D22, 2 samples for D24 and 2 samples for D26.

The raw sequencing data (FASTQ files) were aligned to the UCSC mm10 mouse genome using the STAR software (version 2.7.11b) (Dobin et al. 2013) to generate BAM files. Raw read counts were extracted from the BAM files using HTSeq (version 2.0.5) (Anders et al. 2015) with the following parameters: -t exon, -f bam, -r pos, --stranded=reverse, -m intersection-strict, and --nonunique none.

Normalization of read counts was performed using the DESeq2 R package (version 1.22.2) (Anders and Huber 2010; Love et al. 2014). Counts were transformed into DESeq2-normalized values and subsequently log-transformed using the formula log2(1 + DESeq2-normalized counts). Differential expression analysis was conducted with the R package "SARTools" (Varet et al. 2016).

Purified RNA from fractionated round spermatids were also sequenced to establish gene transcriptional group quartile used shown in Fig. 4. RNA purification and sequencing were performed as described above.

Quantification and statistical analysis

Statistical analysis was performed with R and GraphPad Prism 8. The results of fertility tests were analyzed by Student t-test. Pairwise Student t-test was used to analyze testis weights and spermatozoa counts of same-aged mice and ratio pairwise Student t-test was used for the IVF efficiency results. The results of sperm decompaction test were analyzed by two-way ANOVA and Tukey's HSD post two-way ANOVA test was used to determine the significance between groups. *P-values* < 0.05 were considered statistically significant: $*p < 0.05$, $**p < 0.01$, $***p < 0.001$.

Gene Set Enrichment Analysis (GSEA)

Differential expression analysis and the corresponding GSEA analysis (Mootha et al. 2003; Subramanian et al. 2005) were performed to compare *Atad2* KO versus *Atad2* wild-type samples at days 20, 22, 24, and 26 PP. For the GSEA analysis, we used the Python package "gseapy" (Fang et al. 2023) available at https://www.gsea-msigdb.org/gsea.

The GSEA was carried out on three custom gene sets. The first gene set, referred to as "sex chromosome-linked genes", corresponds to genes located on the X and Y chromosomes. The remaining two gene sets include genes identified as upregulated or downregulated in the

absence of histone H3.3 by Fontaine and colleagues (Fontaine et al. 2022). These gene sets were designated as "post-meiotic H3.3-activated genes" and "post-meiotic H3.3-repressed genes", respectively.

Data availability

The transcriptomic data generated in this study, corresponding to testes collected at different days post-partum, have been deposited on GEO under the accession N°. GSE277943.

To review GEO accession GSE277943 go to :

https://www.ncbi.nlm.nih.gov/geo/query/acc.cgi?acc=GSE277943

Enter token wrszesqgjfkxxmx into the box.

Transcriptomic data from fractionated round spermatids (three biological replicates, Fig. 4A) were deposited on GEO accession GSE284749. To review GEO accession GSE277943 go to:

https://www.ncbi.nlm.nih.gov/geo/query/acc.cgi?acc=GSE284749.

Enter token uzmvcaygpnydrgt into the box

ATAC-seq data generated in this study were deposited on GEO under the accession N° GSE283879. To review GEO accession GSE283879, go to :

https://www.ncbi.nlm.nih.gov/geo/query/acc.cgi?acc=GSE283879

Enter token ozazwsmoxjofzkb into the box

Immunoblot raw data used in preparing the figures are presented as **Supplementary file 1**

Manuscript preparation

Parts of the text have been refined, with the help of free online tools (ChatGPT and DeepL).

COMPETING INTEREST STATEMENT

The authors declare that they have no conflict of interest.

ACKNOWLEDGEMENTS

This work was supported by ANR EpiSperm 4 (ANR-19-CE12- 0014), ANR Episperm 5 (ANR-23-CE12-0028), ANR NME-CoA (ANR-23-CE14-0050) and the Cancer ITMO [Multi-Organization Thematic Institute of the French Alliance for Life Sciences and Health (AVIESAN)] MIC program

to SK and SR. AL is a recipient of a 4th year PhD fellowship by Foundation pour la Recherche Médicale (FRM). High throughput sequencing was performed at the TGML Platform, supported by grants from Inserm, GIS IBiSA, Aix-Marseille Université. We thank Dr. Alexandra Varga for X-gal staining of testis sections. The authors thank Dr Kelly Matmati, Stroke Program Director, Rochester General Hospital, Connecticut, USA, for her critical reading of the manuscript.

AUTHOR CONTRIBUTIONS

AL: experimentation, data interpretation, writing and preparation of the manuscript, FB: supervision, experimentation, data interpretation, writing and preparation of the manuscript, management of acquisition of *Atad2* KO mouse model. SB: experimentation and the maintain of *Atad2* mouse model, EL and CA *in vitro* fertilization essays. FC and EBF transcriptomic data analyses. DePu and CG: transcriptomic data generation, SR: founding acquisition and transcriptomic analysis. DaPe and AV: experimentation and data generation and analyses. SK: conception, founding acquisition and supervision, and coordination of the whole project and writing of the manuscript.

Figure legends

Liakopoulou_Fig1

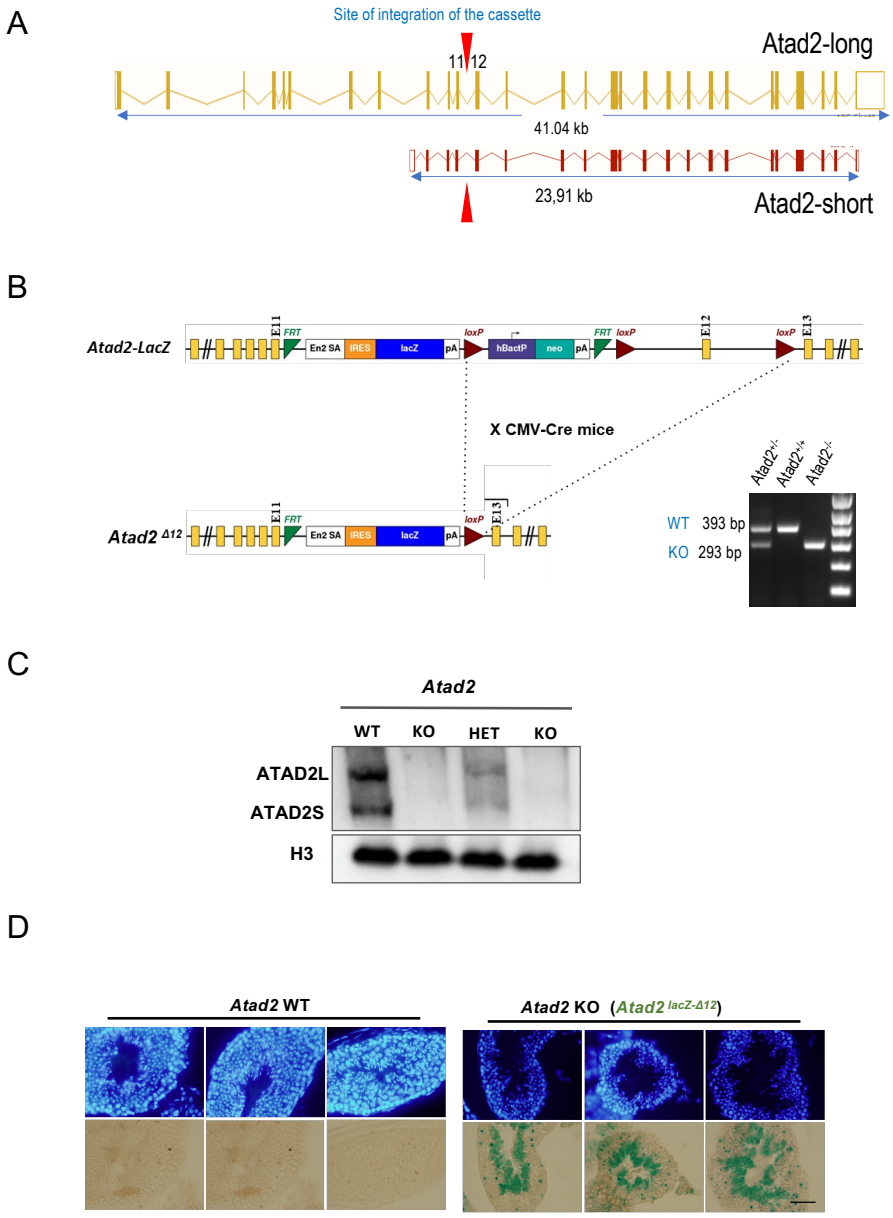

Figure 1: Atad2 is highly expressed in post-meiotic male germ cells.

(**A**) The exon/intron organization of *Atad2* gene and the two ATAD2-encoding transcriptional units (encoding for ATAD2-long and ATAD2-short) are indicated (Dyer et al. 2025). The red arrows indicate the position of insertion of the *Lac-Z-Lox-Neo-Lox* cassette.

(**B**) Gene targeting strategy for the generation of the *Atad2* KO allele is represented. Exon number and relative position, selection gene cassettes, LoxP sites and Frt sites are indicated.

Crossing mice bearing this construct with *CMV-Cre* mice resulted in the generation of the *Atad2 LacZ*$^{\Delta Neo\text{-}Exon12}$ allele, which can be verified through PCR amplification of the genomic DNA (shown on the ethidium bromide-stained gel). The expected amplified bands for each genotype allowing the detection of both wild-type and KO alleles of *Atad2* are indicated. E = Exon.

(**C**) Extracts from wild-type and *Atad2* KO mice testes were probed with anti-ATAD2 and anti-H3 antibodies as indicated. Four different mice were used for this experiment.

(**D**) Seminiferous tubules sections from wild-type and *Atad2* KO mice were stained with X-gal to visualize *lacZ* gene expression and β -galactosidase activity under the endogenous *Atad2* gene promoter. Testes from three different wild-type and *Atad2* KO mice were used to generate the represented sections. Scale bar: 200 µm

Liakopoulou_Fig2

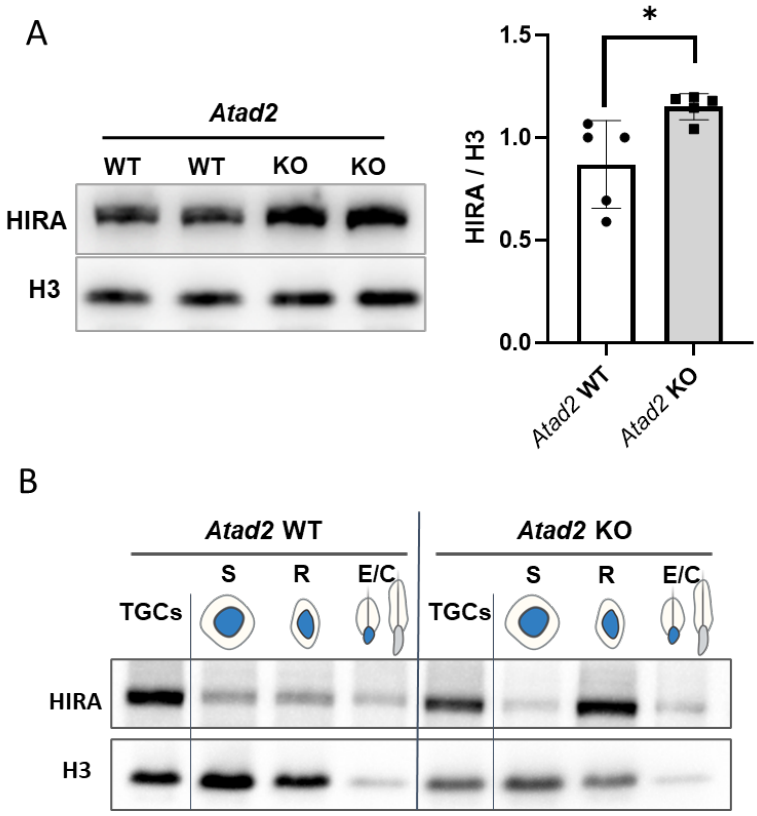

Figure 2: *Atad2* gene inactivation leads to the accumulation of HIRA

(**A**) Total testes' extracts from individual wild-type or Atad2 KO mice (n =5) were used to detect HIRA and H3 by immunoblotting. The panel shows a representative immunoblotting after HIRA detection. The histogram shown in the lower left panel represents quantification of HIRA immunoblotting signal normalized to H3. Mean ± Standard Deviation is 0.86± 0.21 and 1.15± 0.06 for wild type and *Atad2* KO samples respectively and the p value is 0.02 for unpaired Student t-test.

(**B**) Extracts from fractionated spermatogenic cells (pool of testes from 3 individuals per genotype) were used to detect HIRA and H3.

Liakopoulou_Fig3

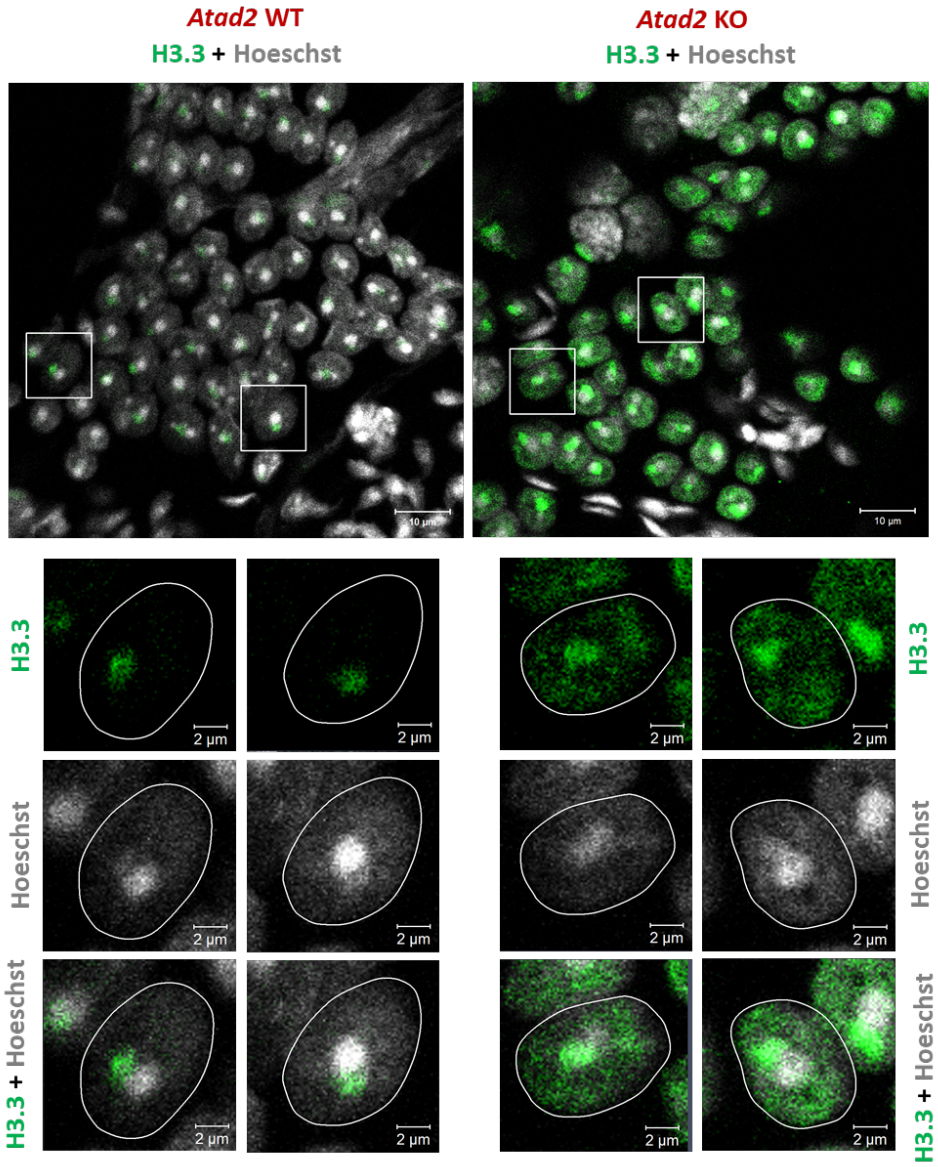

Figure 3: Enhanced H3.3 detection in *Atad2* KO post-meiotic cells

A specific antibody against H3.3 was used to detect H3.3 in round spermatid cells from WT and *Atad2* KO mice. Round spermatids are recognizable by their distinctive Hoechst - bright chromocenter (upper panels). The lower panels represent the magnification of selected cells shown at a lower magnification in the upper panels. The images show H3.3 labelling and Hoechst staining alone or the merged images of these staining as indicated.

Liakopoulou_Fig4

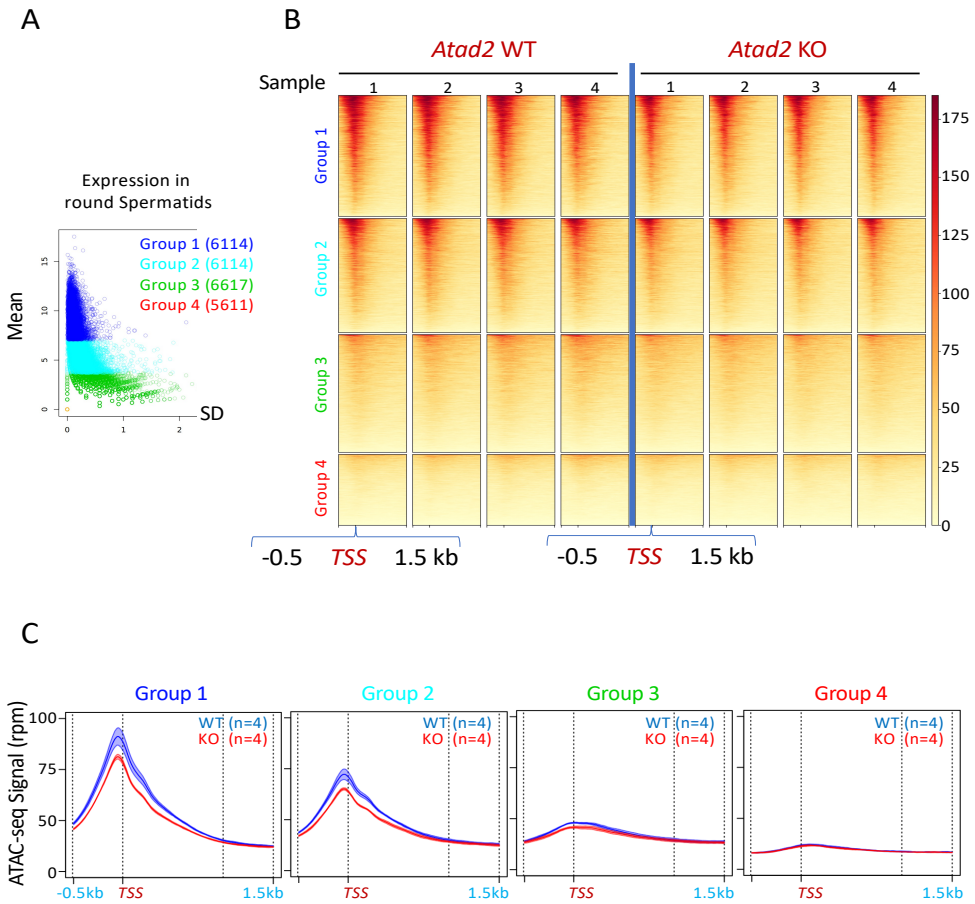

Fig. 4: ATAD2 controls active gene TSS accessibility

A) Gene selection according to expression in round spermatids. The plot displays the mean expression levels on the y-axis and the corresponding standard deviations on the x-axis, calculated from three independent biological replicates of isolated round spermatids. The genes were divided into 4 groups (grp1 in blue, grp2 in cyan, grp3 in green and grp4 in orange) according to the quartile of their mean expression.

B) Heatmap on ATAC-seq signal. The heatmap shows the ATAC-seq signal of each group (grp1 in blue, grp2 in cyan, grp3 in green and grp4 in orange) in rows, for 4 ATAD2 WT and 4 ATAD2 KO samples in column.

C) Profiles according to selected genes. The panels show for each group the mean profile

(± 2 s.e.m) (solid line) of four ATAD2 WT replicates (in blue) and 4 ATAD2 KO (in red) (transparency) over the four replicates.

Liakopoulou_Fig5

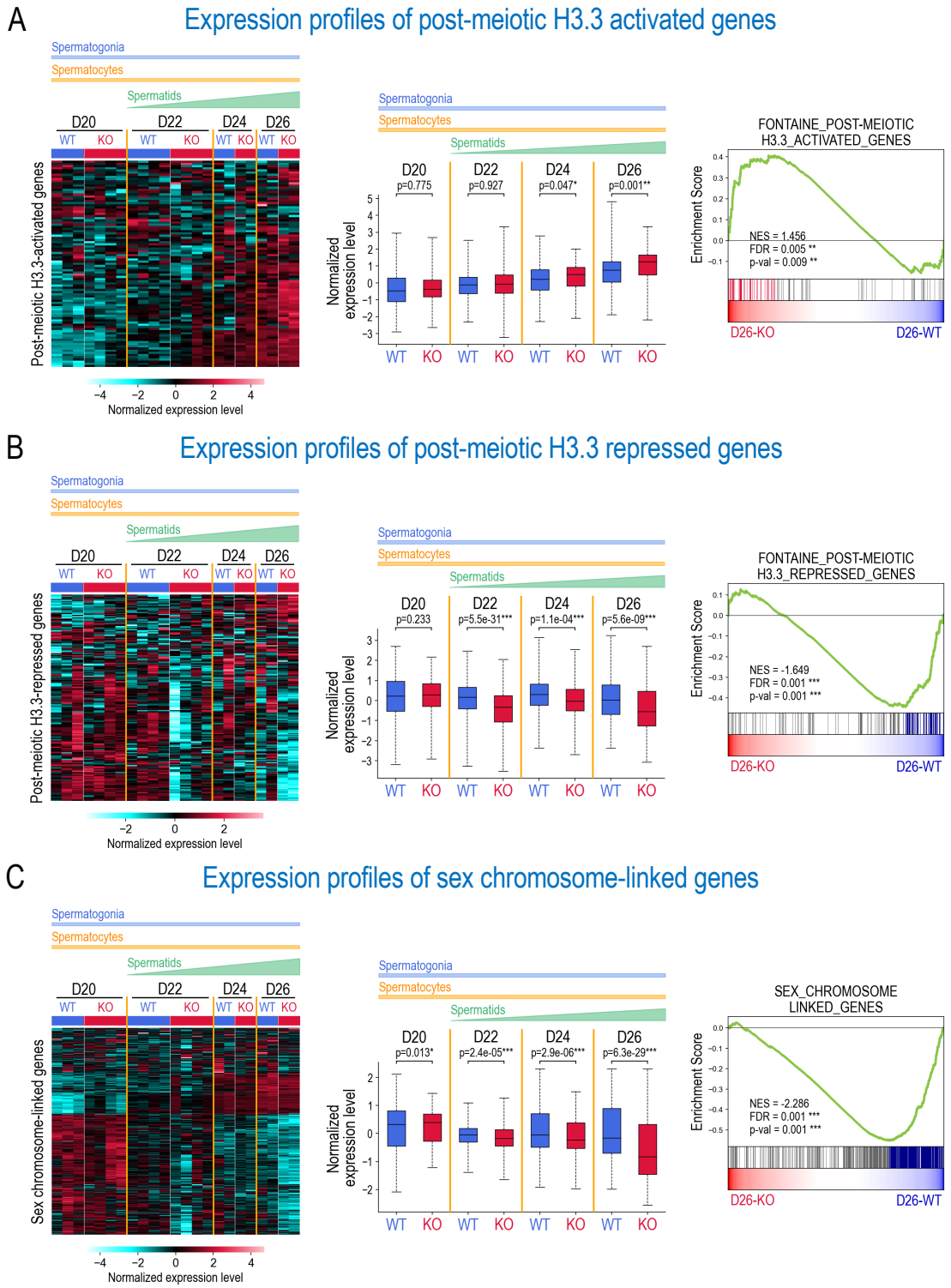

Figure 5: ATAD2 enhances H3.3 gene regulatory functions.

(A) Expression profiles of post-meiotic H3.3-activated genes. The heatmap (left panel) displays the normalized expression levels of genes identified by Fontaine and colleagues as upregulated in the absence of histone H3.3, (Fontaine et al. 2022) for ATAD2 WT and ATAD2 KO samples at days 20, 22, 24, and 26 PP. The colour scale represents the z-score of log-transformed DESeq2-normalized counts. The box plots (middle panel) show the pooled normalized expression levels, aggregated across replicates and genes, for each condition (WT and KO) and time point (D20 to D26). Statistical significance between WT and KO conditions was determined using a two-sided t-test, with p-values indicated as follows: * for p-value<0.05, ** for p-value<0.01, *** for p-value<0.001. The GSEA results (right panel) highlight a significant enrichment of the "post-meiotic H3.3-activated genes" gene set in KO samples relative to WT samples at D26. The coloured vertical bars represent the core genes that account for the gene set's enrichment signal.

(B) As in (A) for the "post-meiotic H3.3-repressed genes" gene set.

(C) As in (A) for the " sex chromosome-linked genes " gene set.

Liakopoulou_Fig.6

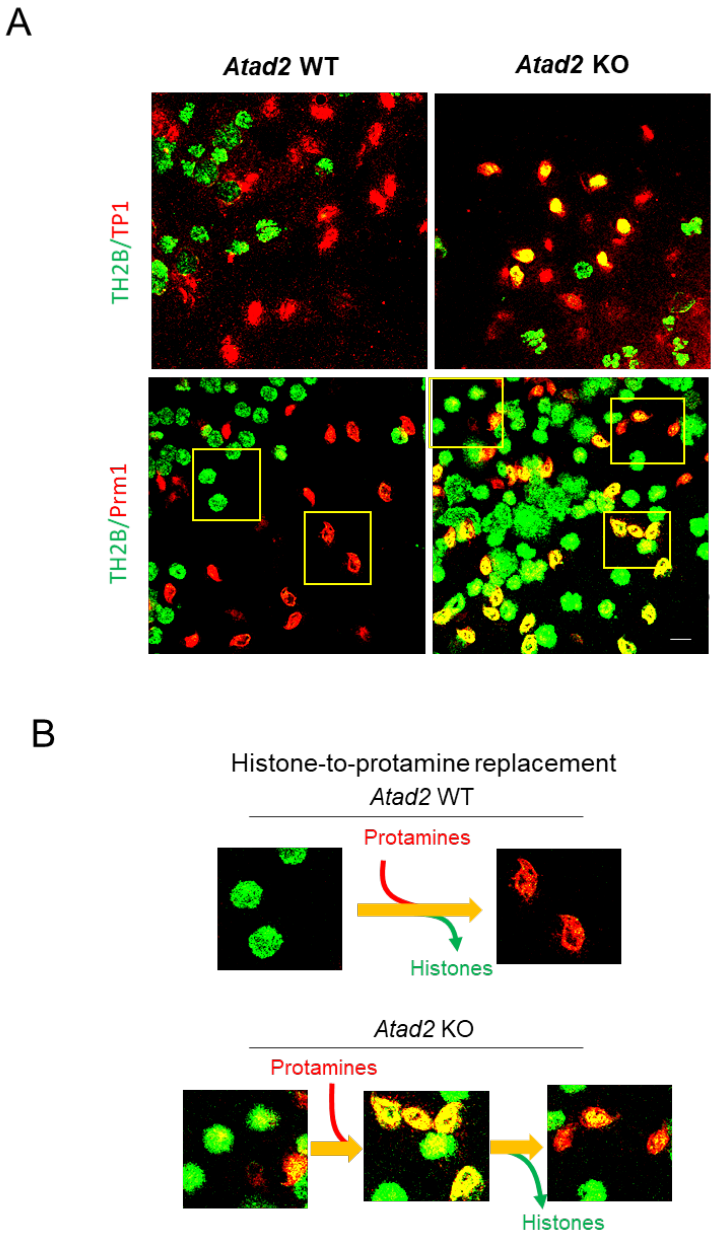

Figure 6: Atad2 is required for efficient histone-to-protamine replacement.

(**A**) Spermatogenic cell preparations from wild-type and *Atad2* KO mice were stained with antibodies against TH2B (in green) and transition protein 1 (TP1) or protamine 1 (PRM1) (in red). A yellow signal indicates the co-detection of TH2B along with TP1 or PRM1. The indicated fields are shown at higher magnification in panel "B". Scale bar: 10 µm.

(**B**) Fields shown in panel "A" are ordered to illustrate the transition from the histone associated genome to its packaging by protamines, considering both wild-type and *Atad2* KO spermatogenic cells.

Liakopoulou_Fig. 7

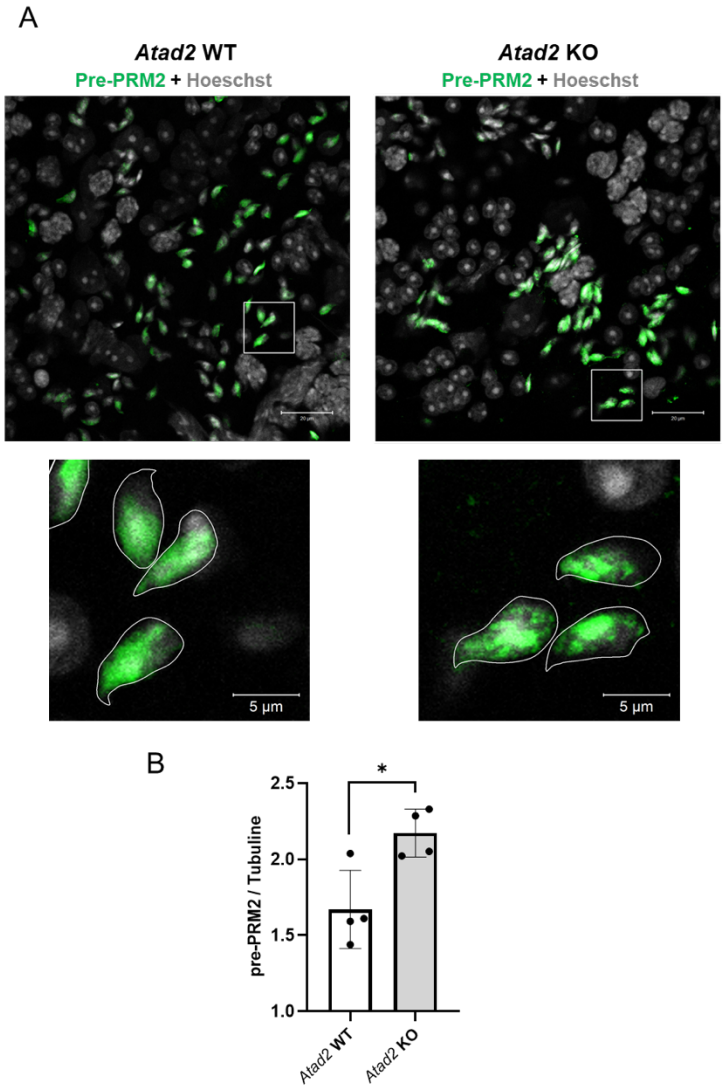

Figure 7: Atad2 is required for proper pre-protamine 2 processing and protamine assembly

(**A**) A specific antibody raised against the processed part of pre-PRM2 (Rezaei-Gazik et al. 2022) was used to detect pre-PRM2 expression and localization in tubular elongating spermatid cells. The lower panels represent the magnification of selected cells.

(**B**) The amount of pre-PRM2 was detected using soluble extracts from testis of wild-type and *Atad2* KO mice using ELISA. Histograms show the normalized values (pre-PRM2/tubulin) of 4 measurements of sedimentation samples of Elongating/Condensing fractions. Mean ± Standard Deviation is 1.6 ± 0.2 and 2.1 ± 0.1 for wild type and *Atad2* KO samples respectively and the p value equals 0.0158 when applying unpaired Student t-test.

Liakopoulou_Fig8

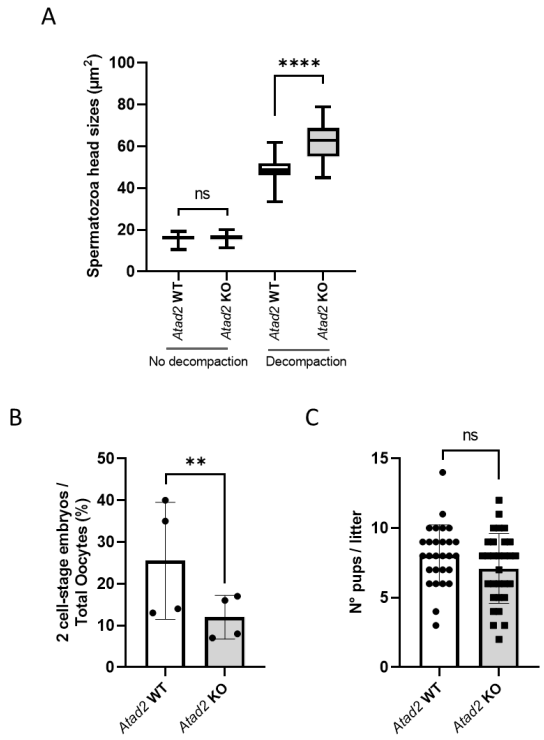

Figure 8: ATAD2s' function in sperm genome compaction and fertility parameters

(**A**) Epididymal sperm cells were isolated by the swim-up method from wild-type or *Atad2* KO mice and underwent a decompaction test and the sizes of the sperm heads were measured and represented as box plots (*n* = 75 sperm heads / box plot). The value ranges (mean) were 10.4 ~ 19.3 (16.0) for wild type sperms without decompaction; 11.4 ~ 20.1 (16.4) for *Atad2* KO sperms without decompaction; 33.4 ~ 61.8 (48.5) for wild type sperms after decompaction; 45.0 ~ 78.9 (62.6) *Atad2* KO sperms after decompaction. Tukey's HSD post two-way ANOVA test was used. ****$p < 0.001$.

(**B**) Pools of oocytes from C57BL6 females were obtained and used for *in vitro* fertilization (IVF) with spermatozoa from WT or *Atad2* KO males (the experiment was repeated 4 times independently). The fertilization success rate is indicated as a percentage of oocytes giving rise to stage 2 embryos. Mean ± Standard Deviation is 25.5 ± 14 and 12 ± 5.2 for wild type and *Atad2* KO experiments respectively and the p = 0.002 for ratio paired Student t-test.

(**C**) Wild-type (*n* = 5) and *Atad2* KO (*n* = 5) male mice were crossed with C57BL6 female mice and the number of pups was counted and reported as box plots (*n* = 28 and 30, respectively). The average numbers of pups are respectively 8.0 ± 2.1 and 7.1 ± 2.5 and the *p-value of* Student t-test = 0.1.

REFERENCES

Anders S, Huber W. 2010. Differential expression analysis for sequence count data. *Genome Biol* **11**: R106.

Anders S, Pyl PT, Huber W. 2015. HTSeq--a Python framework to work with high-throughput sequencing data. *Bioinformatics* **31**: 166-169.

Bao J, Bedford MT. 2016. Epigenetic regulation of the histone-to-protamine transition during spermiogenesis. *Reproduction* **151**: R55-70.

Barral S, Morozumi Y, Hoghoughi N, Rousseaux S, Khochbin S. 2017a. [The mystery of histone disappearance during spermatogenesis]. *Med Sci (Paris)* **33**: 588-590.

Barral S, Morozumi Y, Tanaka H, Montellier E, Govin J, de Dieuleveult M, Charbonnier G, Coute Y, Puthier D, Buchou T et al. 2017b. Histone Variant H2A.L.2 Guides Transition Protein-Dependent Protamine Assembly in Male Germ Cells. *Mol Cell* **66**: 89-101 e108.

Bashiri Z, Amidi F, Amiri I, Zandieh Z, Maki CB, Mohammadi F, Amiri S, Koruji M. 2021. Male Factors: the Role of Sperm in Preimplantation Embryo Quality. *Reprod Sci* **28**: 1788-1811.

Boussouar F, Jamshidikia M, Morozumi Y, Rousseaux S, Khochbin S. 2013. Malignant genome reprogramming by ATAD2. *Biochim Biophys Acta* **1829**: 1010-1014.

Caron C, Lestrat C, Marsal S, Escoffier E, Curtet S, Virolle V, Barbry P, Debernardi A, Brambilla C, Brambilla E et al. 2010. Functional characterization of ATAD2 as a new cancer/testis factor and a predictor of poor prognosis in breast and lung cancers. *Oncogene* **29**: 5171-5181.

Cattaneo M, Morozumi Y, Perazza D, Boussouar F, Jamshidikia M, Rousseaux S, Verdel A, Khochbin S. 2014. Lessons from yeast on emerging roles of the ATAD2 protein family in gene regulation and genome organization. *Mol Cells* **37**: 851-856.

de Dieuleveult M, Yen K, Hmitou I, Depaux A, Boussouar F, Bou Dargham D, Jounier S, Humbertclaude H, Ribierre F, Baulard C et al. 2016. Genome-wide nucleosome specificity and function of chromatin remodellers in ES cells. *Nature* **530**: 113-116.

Dobin A, Davis CA, Schlesinger F, Drenkow J, Zaleski C, Jha S, Batut P, Chaisson M, Gingeras TR. 2013. STAR: ultrafast universal RNA-seq aligner. *Bioinformatics* **29**: 15-21.

Dyer SC, Austine-Orimoloye O, Azov AG, Barba M, Barnes I, Barrera-Enriquez VP, Becker A, Bennett R, Beracochea M, Berry A et al. 2025. Ensembl 2025. *Nucleic Acids Res* **53**: D948-D957.

Fang Z, Liu X, Peltz G. 2023. GSEApy: a comprehensive package for performing gene set enrichment analysis in Python. *Bioinformatics* **39**.

Fontaine E, Papin C, Martinez G, Le Gras S, Nahed RA, Hery P, Buchou T, Ouararhni K, Favier B, Gautier T et al. 2022. Dual role of histone variant H3.3B in spermatogenesis: positive regulation of piRNA transcription and implication in X-chromosome inactivation. *Nucleic Acids Res* **50**: 7350-7366.

Gaucher J, Reynoird N, Montellier E, Boussouar F, Rousseaux S, Khochbin S. 2010. From meiosis to postmeiotic events: the secrets of histone disappearance. *FEBS J* **277**: 599-604.

Gaucher JF, Mauge C, Didry D, Guichard B, Renault L, Carlier MF. 2012. Interactions of isolated C-terminal fragments of neural Wiskott-Aldrich syndrome protein (N-WASP) with actin and Arp2/3 complex. *J Biol Chem* **287**: 34646-34659.

Goudarzi A, Zhang D, Huang H, Barral S, Kwon OK, Qi S, Tang Z, Buchou T, Vitte AL, He T et al. 2016. Dynamic Competing Histone H4 K5K8 Acetylation and Butyrylation Are Hallmarks of Highly Active Gene Promoters. *Mol Cell* **62**: 169-180.

Hammond CM, Bao H, Hendriks IA, Carraro M, Garcia-Nieto A, Liu Y, Reveron-Gomez N, Spanos C, Chen L, Rappsilber J et al. 2021. DNAJC9 integrates heat shock molecular chaperones into the histone chaperone network. *Mol Cell* **81**: 2533-2548 e2539.

Hoghoughi N, Barral S, Vargas A, Rousseaux S, Khochbin S. 2018. Histone variants: essential actors in male genome programming. *J Biochem* **163**: 97-103.

Jang J, Kang Y, Zofall M, Cho C, Grewal S, Lee JY. 2024. Abo1 ATPase facilitates the dissociation of FACT from chromatin. *bioRxiv*.

Krastev DB, Li S, Sun Y, Wicks AJ, Hoslett G, Weekes D, Badder LM, Knight EG, Marlow R, Pardo MC et al. 2022. The ubiquitin-dependent ATPase p97 removes cytotoxic trapped PARP1 from chromatin. *Nat Cell Biol* **24**: 62-73.

Lafon A, Taranum S, Pietrocola F, Dingli F, Loew D, Brahma S, Bartholomew B, Papamichos-Chronakis M. 2015. INO80 Chromatin Remodeler Facilitates Release of RNA Polymerase II from Chromatin for Ubiquitin-Mediated Proteasomal Degradation. *Mol Cell* **60**: 784-796.

Langmead B, Salzberg SL. 2012. Fast gapped-read alignment with Bowtie 2. *Nat Methods* **9**: 357-359.

Le Blevec E, Muronova J, Ray PF, Arnoult C. 2020. Paternal epigenetics: Mammalian sperm provide much more than DNA at fertilization. *Mol Cell Endocrinol* **518**: 110964.

Lin CJ, Koh FM, Wong P, Conti M, Ramalho-Santos M. 2014. Hira-mediated H3.3 incorporation is required for DNA replication and ribosomal RNA transcription in the mouse zygote. *Dev Cell* **30**: 268-279.

Liu H, Wen Q, Yan S, Zeng W, Zou Y, Liu Q, Zhang G, Zou J, Zou X. 2022. Tumor-Promoting ATAD2 and Its Preclinical Challenges. *Biomolecules* **12**.

Love MI, Huber W, Anders S. 2014. Moderated estimation of fold change and dispersion for RNA-seq data with DESeq2. *Genome Biol* **15**: 550.

Montellier E, Boussouar F, Rousseaux S, Zhang K, Buchou T, Fenaille F, Shiota H, Debernardi A, Hery P, Curtet S et al. 2013. Chromatin-to-nucleoprotamine transition is controlled by the histone H2B variant TH2B. *Genes Dev* **27**: 1680-1692.

Mootha VK, Lindgren CM, Eriksson KF, Subramanian A, Sihag S, Lehar J, Puigserver P, Carlsson E, Ridderstrale M, Laurila E et al. 2003. PGC-1alpha-responsive genes involved in oxidative phosphorylation are coordinately downregulated in human diabetes. *Nat Genet* **34**: 267-273.

Moriniere J, Rousseaux S, Steuerwald U, Soler-Lopez M, Curtet S, Vitte AL, Govin J, Gaucher J, Sadoul K, Hart DJ et al. 2009. Cooperative binding of two acetylation marks on a histone tail by a single bromodomain. *Nature* **461**: 664-668.

Morozumi Y, Boussouar F, Tan M, Chaikuad A, Jamshidikia M, Colak G, He H, Nie L, Petosa C, de Dieuleveult M et al. 2016. Atad2 is a generalist facilitator of chromatin dynamics in embryonic stem cells. *J Mol Cell Biol* **8**: 349-362.

Nashun B, Hill PW, Smallwood SA, Dharmalingam G, Amouroux R, Clark SJ, Sharma V, Ndjetehe E, Pelczar P, Festenstein RJ et al. 2015. Continuous Histone Replacement by Hira Is Essential for Normal Transcriptional Regulation and De Novo DNA Methylation during Mouse Oogenesis. *Mol Cell* **60**: 611-625.

Okada Y. 2022. Sperm chromatin condensation: epigenetic mechanisms to compact the genome and spatiotemporal regulation from inside and outside the nucleus. *Genes Genet Syst* **97**: 41-53.

Puumalainen MR, Lessel D, Ruthemann P, Kaczmarek N, Bachmann K, Ramadan K, Naegeli H. 2014. Chromatin retention of DNA damage sensors DDB2 and XPC through loss of p97 segregase causes genotoxicity. *Nat Commun* **5**: 3695.

Ramirez F, Dundar F, Diehl S, Gruning BA, Manke T. 2014. deepTools: a flexible platform for exploring deep-sequencing data. *Nucleic Acids Res* **42**: W187-191.

Rezaei-Gazik M, Vargas A, Amiri-Yekta A, Vitte AL, Akbari A, Barral S, Esmaeili V, Chuffart F, Sadighi-Gilani MA, Coute Y et al. 2022. Direct visualization of pre-protamine 2 detects protamine assembly failures and predicts ICSI success. *Mol Hum Reprod* **28**.

Rousseaux S, Reynoird N, Khochbin S. 2022. NUT Is a Driver of p300-Mediated Histone Hyperacetylation: From Spermatogenesis to Cancer. *Cancers (Basel)* **14**.

Shiota H, Barral S, Buchou T, Tan M, Coute Y, Charbonnier G, Reynoird N, Boussouar F, Gerard M, Zhu M et al. 2018. Nut Directs p300-Dependent, Genome-Wide H4 Hyperacetylation in Male Germ Cells. *Cell Rep* **24**: 3477-3487 e3476.

Skarnes WC, Rosen B, West AP, Koutsourakis M, Bushell W, Iyer V, Mujica AO, Thomas M, Harrow J, Cox T et al. 2011. A conditional knockout resource for the genome-wide study of mouse gene function. *Nature* **474**: 337-342.

Subramanian A, Tamayo P, Mootha VK, Mukherjee S, Ebert BL, Gillette MA, Paulovich A, Pomeroy SL, Golub TR, Lander ES et al. 2005. Gene set enrichment analysis: a knowledge-based approach for interpreting genome-wide expression profiles. *Proc Natl Acad Sci U S A* **102**: 15545-15550.

Tang MC, Jacobs SA, Mattiske DM, Soh YM, Graham AN, Tran A, Lim SL, Hudson DF, Kalitsis P, O'Bryan MK et al. 2015. Contribution of the two genes encoding histone variant h3.3 to viability and fertility in mice. *PLoS Genet* **11**: e1004964.

van den Berg SJW, East S, Mitra S, Jansen LET. 2023. p97/VCP drives turnover of SUMOylated centromeric CCAN proteins and CENP-A. *Mol Biol Cell* **34**: br6.

van den Boom J, Wolf M, Weimann L, Schulze N, Li F, Kaschani F, Riemer A, Zierhut C, Kaiser M, Iliakis G et al. 2016. VCP/p97 Extracts Sterically Trapped Ku70/80 Rings from DNA in Double-Strand Break Repair. *Mol Cell* **64**: 189-198.

van der Heijden GW, Derijck AA, Posfai E, Giele M, Pelczar P, Ramos L, Wansink DG, van der Vlag J, Peters AH, de Boer P. 2007. Chromosome-wide nucleosome replacement and H3.3 incorporation during mammalian meiotic sex chromosome inactivation. *Nat Genet* **39**: 251-258.

Varet H, Brillet-Gueguen L, Coppee JY, Dillies MA. 2016. SARTools: A DESeq2- and EdgeR-Based R Pipeline for Comprehensive Differential Analysis of RNA-Seq Data. *PLoS One* **11**: e0157022.

Wang T, Perazza D, Boussouar F, Cattaneo M, Bougdour A, Chuffart F, Barral S, Vargas A, Liakopoulou A, Puthier D et al. 2021. ATAD2 controls chromatin-bound HIRA turnover. *Life Sci Alliance* **4**.

Yuen BT, Bush KM, Barrilleaux BL, Cotterman R, Knoepfler PS. 2014. Histone H3.3 regulates dynamic chromatin states during spermatogenesis. *Development* **141**: 3483-3494.

Supplementary materials

Supplemental_Fig_S1

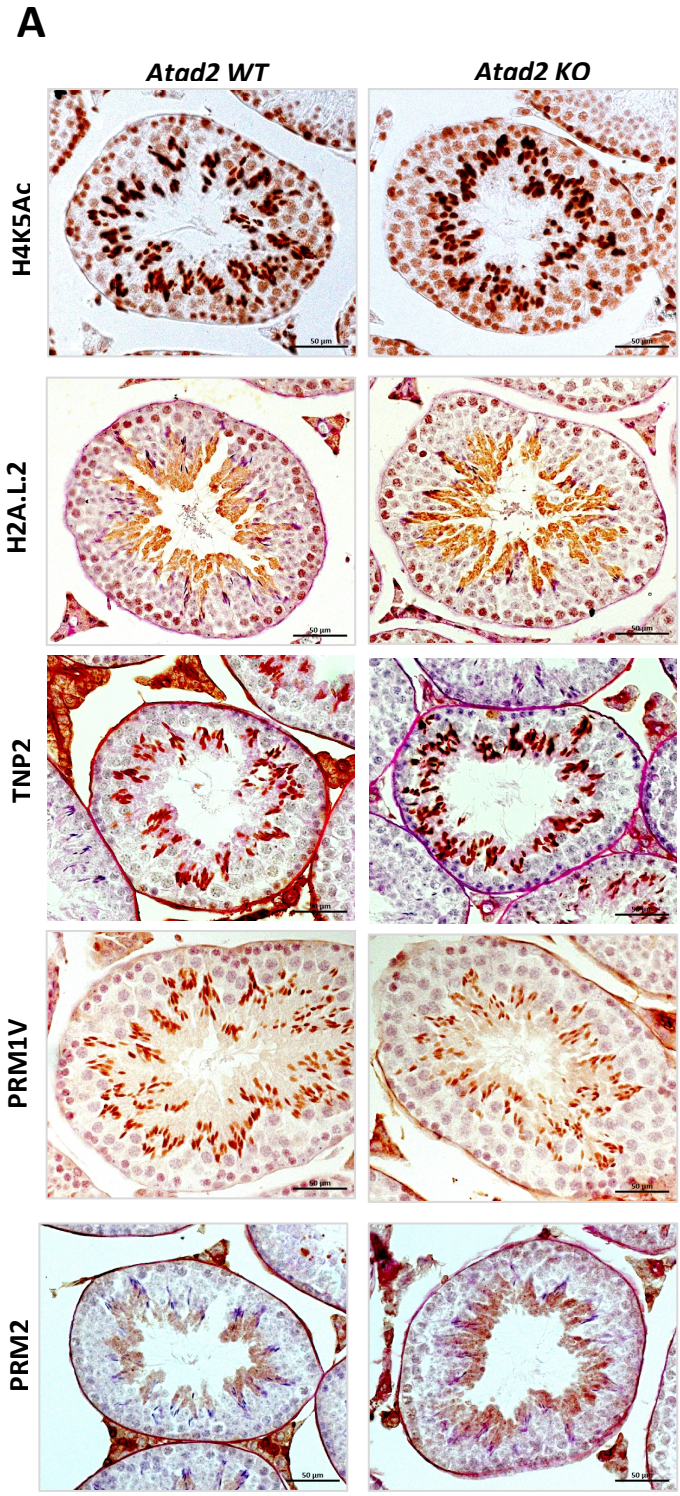

Figure S1: *Atad2* gene inactivation does not significantly disrupt testis histology, the occurrence of H4K5ac, or the cell-specific accumulation of H2A.L.2, TP2, PRM1 and PRM2. Sections of paraffin-embedded testes from wild-type or *Atad2* KO mice were used to visualize the accumulation H4K5ac or expression of H2A.L.2, TP2, PRM1 and PRM2.

Supplemental_Fig_S2

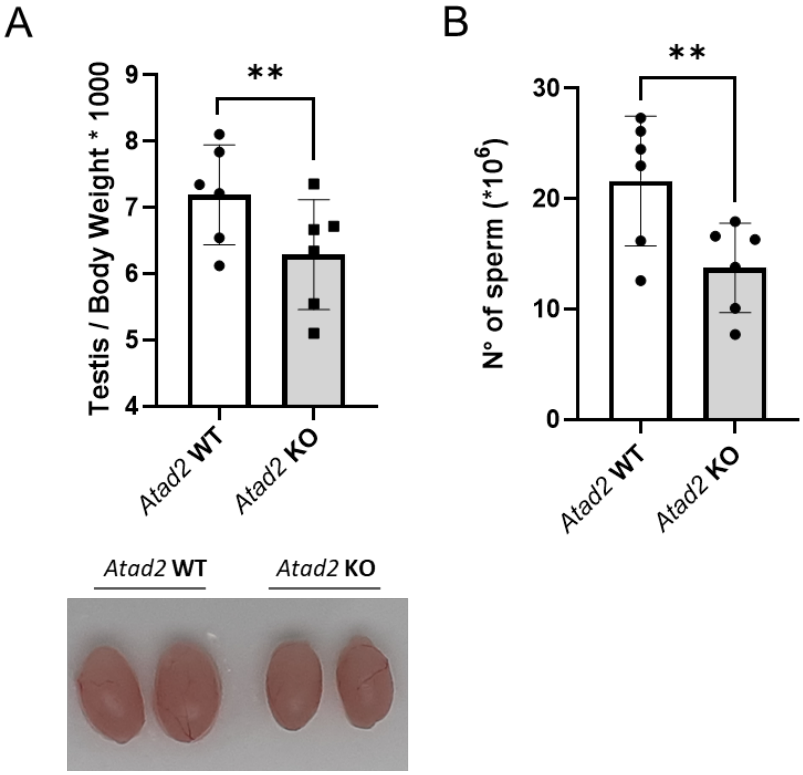

Figure S2: *Atad2* depletion affects testis weight and mature sperm counts.
(**A**) Testes from six 21- to 27-week-old wild-type and *Atad2* KO mice were collected, weighted (mg) and their weights normalized to body weight and only same-age mice were compared pairwise. Histograms represent the mean of the measured weights and error bars the Standard Deviation. The *p*-value of pairwise Student t-test = 0.004 (upper panel). The lower panel shows representative testes from wild-type and *Atad2* KO mice.
(B) Spermatozoa counts (Cells /ml) were performed for pairs of wild type and *Atad2* KO (*n=6*). The average numbers of spermatozoa counts are respectively 21.6 ± 5.8 and 13.7 ± 4,. and the *p*-value of paired Student t-test = 0.001.

Supplemental_Table_S1

Table S1: Primary Antibodies

Name	Company	Reference	Host Species	Dilution
Anti-ATAD2	Homemade	-	Rabbit	1:1000
anti-H2A.L1/L2 SAB771	Homemade	-	Rabbit	1:200 for IHC
Anti-Histone H3 antibody - Nuclear Marker and ChIP Grade	Abcam	Ab1791	Rabbit	1:5000 for WB
Anti-H2B (testis specific)	Abcam	AB178426	Rabbit	1:100 for IF
anti-H3F3B	Abnova	#H00003021-M01	Mouse	1:200 for IF
Anti-H4K5Ac	PTM Biolabs	#PTM-163	Mouse	1:200 for IHC
Anti-HIRA	Cell Signaling Technology	D6O8L	Rabbit	1:1000 for WB
Pre-PRM2	Homemade	-	Rabbit	1:100 for IF
anti-Protamine 1	BRIAR Patch Biosciences	HUP1N	Mouse	1:200 for IHC/IF
anti-Protamine 2	BRIAR Patch Biosciences	HUP2B	Mouse	1:200 for IHC
Anti-TNP2 (B-2)	Santa Cruz Biotechnology	sc-393843	Mouse	1:200 for IHC
Goat anti Rabbit IgG (H + L)-HRP	Bio-rad	Cat# 1706515	-	1:5000 for WB
Goat anti-Mouse IgG (H + L)-HRP	Bio-rad	Cat# 1706516	-	1:5000 for WB
Alexa Fluor™ 568 goat Anti-mouse IgG (H+L)	Invitrogen	Cat# A11004	-	1:500 for IF
Alexa Fluor™ 488 goat Anti-rabbit IgG (H+L)	Invitrogen	Cat# A11034	-	1:500 for IF

WB: Western Blot Analysis, IF: Immunofluorescence and IHC: Immunohistochemistry.

Supplemental_Table_S2

Table S2: Reagents / Products used

Products	Company	Reference
Bovine Serum Albumin (BSA)	Euromedex	# 04-100-812-C
Clarity™ Western ECL Substrate	Bio-Rad	Cat # 170-5061
Clarity Max™ Western ECL Substrate	Bio-Rad	Cat # 170-5062
Complete Protease inhibitor EDTA-free	Sigma-Aldrich	# 4693159001
Dako Fluorescent Mounting Medium	Dako	S3023
DL-Dithiothreitol (DTT)	Euromedex	EU0006
DNase I recombinant	Roche	4536282001
DPBS	Gibco	14200-075
Ethylenediaminetetraacetic acid disodium salt dihydrate (EDTA)	Sigma-Aldrich	E6635
Ethylene glycol-bis (2-aminoethylether)-N,N,N',N'-tetraacetic acid (EGTA)	Sigma-Aldrich	E3889
Formalin solution, neutral buffered, 10%	Sigma-Aldrich	HT5012
Glutaraldehyde solution	Sigma-Aldrich	G5882
Heparin sodium salt from porcine intestinal mucosa	Sigma-Aldrich	H3149
Hoechst	Invitrogen	# 33342
Human Chorionic Gonadotropin (HCG)	MED-VET	Chorulon 1500 UI
Laemmli Sample Buffer 4x	BioRad	# 1610747
Magnesium Chloride (MgCl2)	Euromedex	2189
Mayer's Hematoxylin Solution	Sigma-Aldrich	MHS16
M2 medium	Sigma-Aldrich	M7167
M16 medium	Sigma-Aldrich	M7292
Nitrocellulose Blotting membrane	Amersham™ Protran®	10600015
Nonidet™ P 40 Substitute (NP 40)	Sigma-Aldrich	74385
NuPAGE™ 4-12% Bis-Tris Gel	Invitrogen	NP0335BOX

Potassium Ferricyanide	Sigma-Aldrich	P-8131
Potassium Ferrocyanide	Sigma-Aldrich	P-9387
Pregnant Mare Serum Gonadotropin (PMSG)	MED-VET	Syncro-part PMSG 600 UI
Saccharose	Sigma-Aldrich	S7903
Saponin from quillaja bark	Sigma-Aldrich	S7900
Sodium deoxycholate (NaDoc)	Sigma-Aldrich	D6750
Superfrost®slides	Thermo Scientific™	LCSF05
TMB ELISA Substrate (High Sensitivity)	Abcam	AB171523
Trans-Blot Turbo 5X Transfer Buffer	BioRad	Cat # 10026938
Triton™ X-100	Sigma-Aldrich	T9284
TRIzol™	Thermo Scientific™	# 15596026
TWEEN® 20	Sigma-Aldrich	P7949
Urea	Sigma-Aldrich	U5378
X-Gal	Invitrogen	B1690
96 Well Round (U) Bottom Plate	Thermo Scientific™	# 163320
450 nm Stop Solution for TMB Substrate	Abcam	AB171529